INFRARED THERMOGRAPHY AT LOW TEMPERATURE

Stéphane Roose,[(1)] Jean-François Vandenrijt,[(1)] Gianluca Casarosa,[(2)]

[(1)] Centre Spatial de Liège, Université de Liège, Avenue du Pré Aily, B-4031 Angleur-Liège, Belgium
[(2)] ESTEC, European Space Agency, Keplerlaan 1, PO Box 299, NL-2200 AG Noordwijk, the Netherlands
sroose@uliege.be.

KEYWORDS

Thermography, thermal vacuum test, infrared camera.

ABSTRACT

The present paper reports on investigations aiming to enlarge the temperature measurement range of Infrared Thermographic System to temperatures down to -100°C in thermal vacuum test (TVAC). Replacing a substantial number of thermocouples in by a non-contact thermographic detector during thermal vacuum test, is highly desirable for a center having TVAC and thermal balance test capabilities. It simplifies test integration and multiplies the number of measurement channels. A test configuration has been built in CSL, to measure simultaneously infrared thermographic signals of objects cooled down to -170°C, with different emissivity areas, with a commercial infrared camera. One reports in this paper on

- Care in camera choice, and test configuration
- Test results
- Management of parasite infrared radiation
- Estimated measurement uncertainty (absolute and relative)
- Systematic improvements and precautions to be foreseen in the future.

1. INTRODUCTION

This project aims to investigate to enlarge the temperature measurement range of Infrared Thermographic System to temperatures down to -100°C. The European Space Agency (ESA) owns a thermographic camera system capable to measure object temperature in its thermal vacuum chamber down to -40°C [1][2][3]. Extension to measure objects to -100°C in TVAC chambers is envisaged.
A first step in this study is to choose a commercial camera that allows to realise the objectives, among the criteria one has

- software, image processing capabilities which offers the end-user real-time temperature measurements. Although infrared cameras are radiometers, they will be used as thermometers.
- low Signal to Noise Ratio (SNR) or Noise Equivalent Temperature Difference (NETD) [4]. This requirement allows to discriminate small temperature differences. Consider 2K as a goal.
- re-calibration flexibility
- the most appropriate spectral sensitivity. This requirement is strongly detector technology related. The latter point can only be understood with an assessment of what happens between detected camera signal and object temperature.

2. PHYSICAL BACKGROUND

The infrared thermography relies on the Planck radiation law. An object emits electromagnetic radiation following the Planck radiation law. The spectral distribution and irradiance depend on the object temperature (Fig.1).

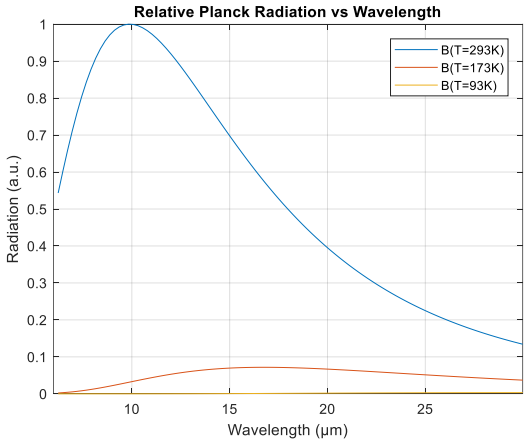

Figure 1: Planck radiation law for object temperature of 293K, 173 K, 93K.

The integrated flux over the wavelength (for a detector with uniform infinite spectral bandwidth) gives the Stefan-Boltzmann law (Fig.2).

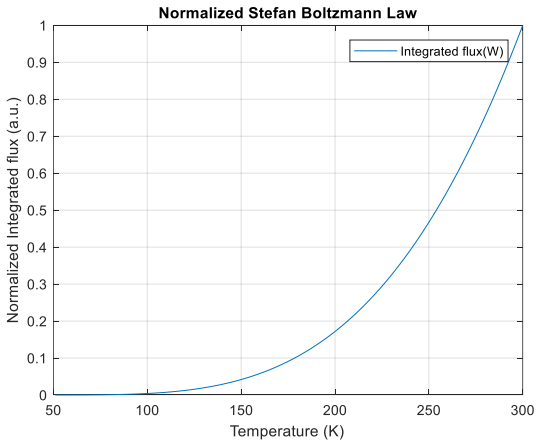

Figure 2: Stefan Boltzmann law.

A thermographic camera measures a “THERMAL FLUX” which is proportional to 2 object characteristics (temperature and surface emissivity). For a given detector, the electronic signal of a pixel “S” is supposed to be proportional to this thermal flux. The proportionality factor depends on pixel size, exposure time, aperture, etc.;

$$S \div \varepsilon.T^4$$

For a camera (detector and its optical imaging system) with uniform spectral response, the uncertainty on the derived temperature depends on the uncertainties “S” and “ε”.

$$T \div (S/\varepsilon)^{1/4}$$
$$\Delta T \div \Delta S/(4.\varepsilon.T^3)$$
$$\Delta T \div T.\Delta\varepsilon/(4.\varepsilon)$$

These formulas are strictly valid if the camera spectral response is flat, which is not the case. But these formulas allow one to understand how detection measurement errors propagate to temperature measurement errors (Fig.3).

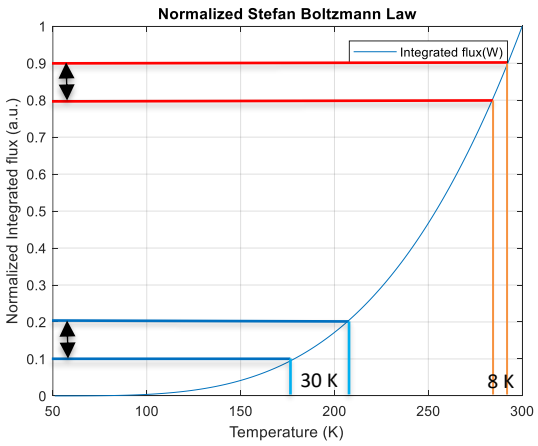

Figure 3: Propagation of a detector signal error ΔS (here=0.1) on the temperature error ΔT.

3. CAMERA TECHNOLOGY SELECTION

Low temperature measurements are sensitive to this error because of the lower slope of the Stefan Boltzmann law (Fig.3) at lower temperature.

$$(dS/dT) \div (4.\varepsilon.T^3)$$

This is unfortunately not improving when considering cameras (detector and optics) with limited spectral bandwidth. Next figure shows three “Gaussian” spectral sensitivities coving MWIR LWIR and VLWIR (Fig.4).
The effect of the spectral limited bandwidths is dramatic because typically for sensitivities limited in the MWIR and LWIR it is accelerating the slope decrease (dS/dT) (Fig.5).

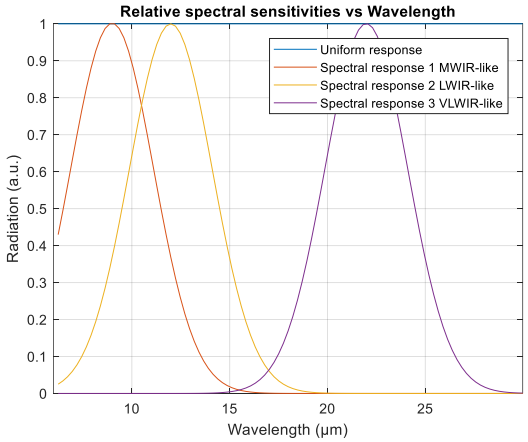

Figure 4: Three “Gaussian” spectral sensitivities covering MWIR LWIR and VLWIR.

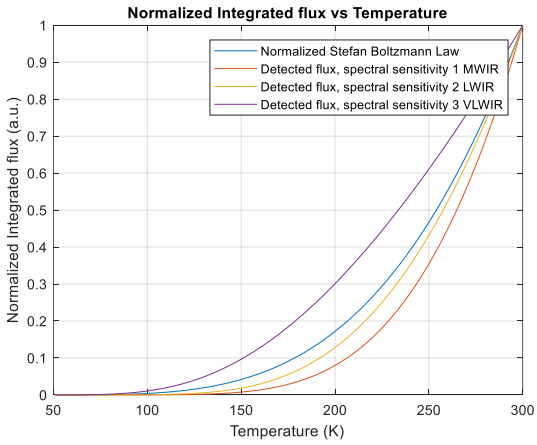

Figure 5: Stefan Boltzmann law corrected for “Gaussian” spectral sensitivities covering MWIR LWIR and VLWIR.

Note that all figures are normalized to 1. Indeed, the object irradiance depend also on the emissivity “ε” of the radiating object (Fig.6, Fig.7).

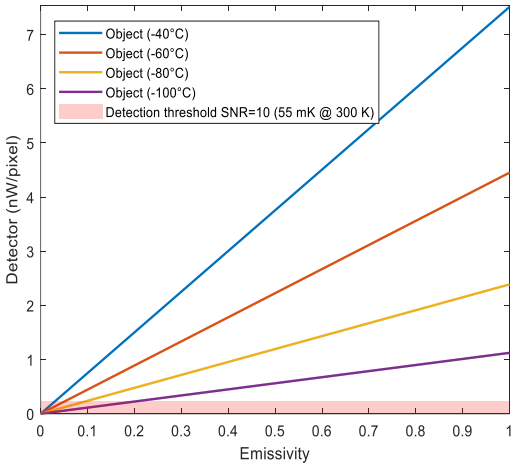

Figure 6: Infrared flux on a detector pixel for various temperature of the object for a LWIR camera. (SNR Threshold for a microbolometer Camera).

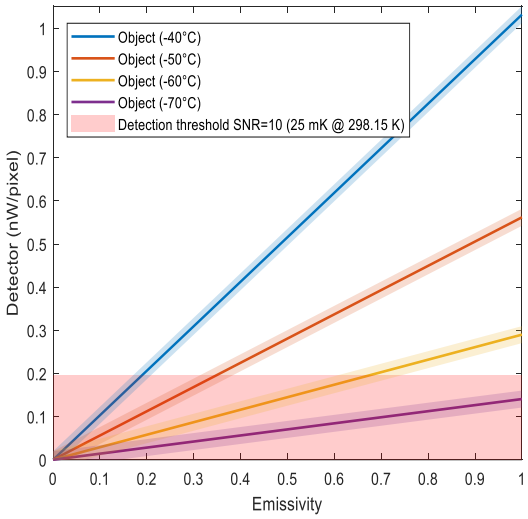

Figure 7: Infrared flux on a detector pixel for various temperature of the object with a MWIR camera. (SNR Threshold for a MWIR Camera)

The lower detection limit depends on the detector SNR. The lower cut-off will define the lowest permissible detection limit (dependent on "ε" too). According to this trade off rules, infrared camera operating in the VLWIR band. Unfortunately, very often these are not thermographic cameras (i.e. cameras calibrated and supported by a software giving a "temperature "read out.)
Our choice turned to an uncooled microbolometer LWIR thermographic cameras and more precisely the INFRATEC VarioCAM (made by Jenoptik) (Fig 8).

Figure 8: INFRATEC VarioCAM HD head 800

4. DEMONSTRATION TEST

4.1. Introduction

The test is fundamentally based on this principle of Fig.9. A test object placed in a thermal vacuum chamber is viewed through a transmission window by an infrared camera. One expects to view the object under test and to record its radiated energy as a grey body (ε<1).
However, the portion of energy radiated by the object and the quantity it reflects, is dependent on its thermo-optical properties as described in Eq.1, which says that:

$$1 = \varepsilon + \rho + \tau \qquad (1)$$

Where,
ε = coefficient of emittance or emissivity
ρ = coefficient of reflection
τ = coefficient of absorption (opaque body τ = 0)

$$\rho = 1 - \varepsilon \qquad (2)$$

A detector pixel measures a signal which is the sum of desired signal (Fig.9) and a sum of parasite fluxes reflected by the object itself (Fig.10) [5] .

S ÷ ε.object flux + (1− ε).(sum of parasite fluxes)

These parasite fluxes appear as an additive flux bias. This means that following Fig.3, the apparent temperature is always higher.

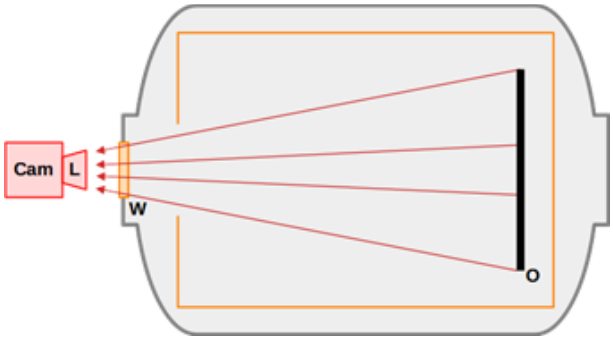

Figure 9: Basic test geometry (desired).

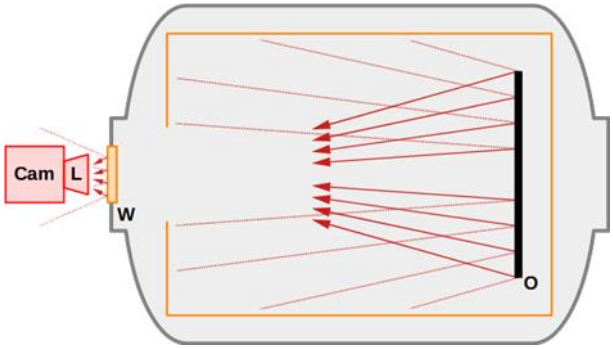

Figure 10: What is also seen by the camera.

The consequences of this are that the measurement feasibility, especially for low emissivity objects (ε<<<1) is not only dependent on good spectral properties of the camera, but also on a knowledge of the test geometry and an evaluation of the level of parasite fluxes in the system.

4.2. Test article

A sample copper plate of 1100 mm x 800 mm, foreseen with piping to allow cooling with GN2 or LN2, and black painted with Chemglaze Z306 [6], was covered with NV14 CERANOVIS white paint and SCOTCH 3M aluminium tape.
The rear side of the shroud was instrumented with 5 mm x 5 mm Pt100 thermistances, located behind the measurement areas.

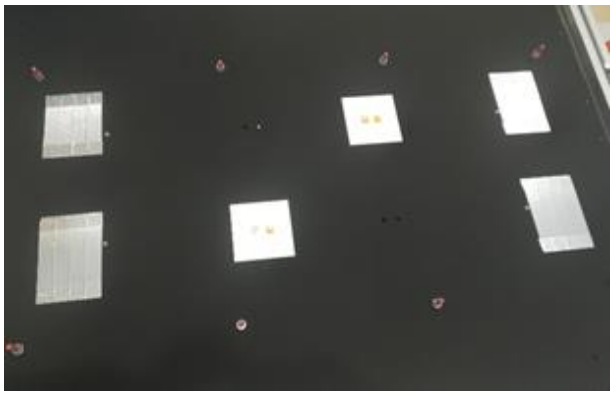

Figure 11: Sample areas with 3 different types of emissivity (Chemglaze Z306, NV14 Ceranovis white paint, Scotch weld 3M Aluminium tape).

4.3. Test configuration

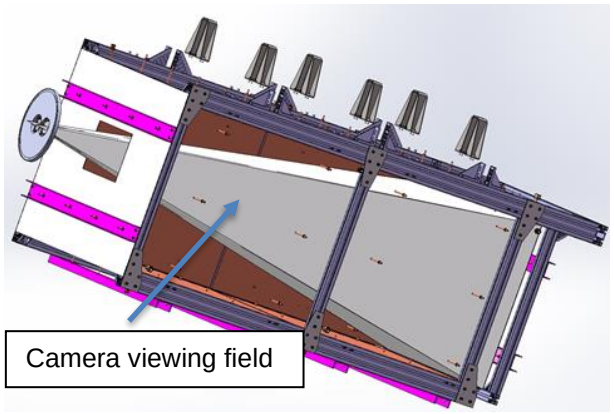

Figure 12: Test geometry: The object shroud (S1) is viewed through a 5-mm thick Zinc Selenide (ZnSe) optical window of CSL's FOCAL2 chamber (Fig.13). The set-up as protected from parasite fluxes at 293K, with a LN2 shroud.

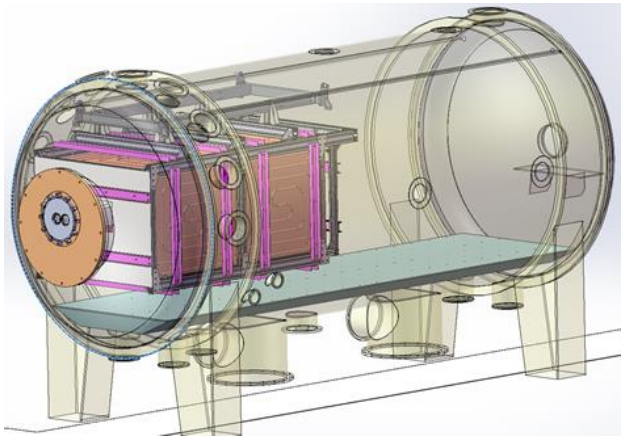

Figure 13: Test geometry shown as mounted in FOCAL 2.

To prevent radiation from the chamber walls to reach the object under test, and be reflected towards the camera, a cold baffle shroud (S3) (LN2 circulation) was built.

The front part of the experiment is a 1100 mm x 800 mm MLI sheet (S5) with a rectangular aperture (S4). It isolates the lid from the object under test from parasite radiation.

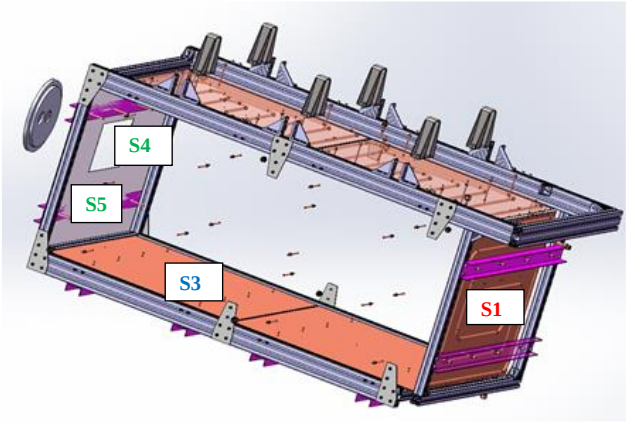

Figure 14: Radiative surfaces (S1,S3,S4,S5) contributing to the detected signal (directly or indirectly) on the camera.

4.4. Parasite flux estimate

Tab.1 gives the level of parasite flux with respect to the object flux. Tab 2. Translates this in a temperature measurement error.

The temperature measurement of low emissivity objects (ε<0.3) are not reliable or very inaccurate in the proposed test configuration. It requires a mandatory subtraction of these parasite signals in the post processing.

Sample object emmissivity	**ε_1=0.3**	**ε_1=0.1**	**ε_1=0.03**
Detected flux	**(pW/pixel)**	**(pW/pixel)**	**(pW/pixel)**
Object at 173 K (-100°C)	**145**	**48**	**15**
Object at 193 K (-80°C)	**314**	**105**	**31**
Object at 213 K (-60°C)	**597**	**199**	**60**
Object at 233 K (-40°C)	**1026**	**342**	**103**
Sum of parasite fluxes	**75.15**	**96.23**	**103.7**
Contribution of the window 295 K (22°C)	0.06	0.06	0.06
Buffer (S3) at 100 K (-173°C)	1.46	1.88	2.02
Front aperture (S4) at 295 K (22°C)	58.57	75.01	80.84
MLI (S5) at 295 K (22°C)	15.06	19.29	20.79

Sample object emmissivity	**ε_1=0.88**	**ε_1=0.7**	**ε_1=0.5**
Detected flux	**(pW/pixel)**	**(pW/pixel)**	**(pW/pixel)**
Object at 173 K (-100°C)	**424**	**337**	**241**
Object at 193 K (-80°C)	**921**	**736**	**524**
Object at 213 K (-60°C)	**1750**	**1400**	**997**
Object at 233 K (-40°C)	**3009**	**2407**	**1714**
Sum of parasite fluxes	**12.88**	**32.12**	**53.47**
Contribution of the window 295 K (22°C)	0.06	0.06	0.06
Buffer (S3) at 100 K (-173°C)	0.25	0.63	1.04
Front aperture (S4) at 295 K (22°C)	10.00	25	41.66
MLI (S5) at 295 K (22°C)	2.57	6.43	10.71

Table 1: Summary Integrated flux seen by a Infratec Variocam (pW/Pixel) and parasite fluxes. Note that the camera (SNR=10) noise level is 40pW/pixel. One considers that measurement is feasible when the object flux exceeds 2 x parasite flux.

Sample object emmissivity	**ε_1=0.3**	**ε_1=0.1**	**ε_1=0.03**
Sum of parasite fluxes (pW/pixel)	**75.15**	**96.23**	**103.7**
Object at 173 K (-100°C)	10K	39K	129K
Object at 193 K (-80°C)	7K	26K	93K
Object at 213 K (-60°C)	5K	18K	69K
Object at 233 K (-40°C)	4K	13K	53K
Object at 293 K (20°C)	2K	5K	27K
Sample object emmissivity	**ε_1=0.88**	**ε_1=0.7**	**ε_1=0.5**
Sum of parasite fluxes (pW/pixel)	**12.88**	**32.12**	**53.47**
Object at 173 K (-100°C)	0.6K	1.8K	4K
Object at 193 K (-80°C)	0.4K	1.3K	3K
Object at 213 K (-60°C)	0.3K	0.9K	2K
Object at 233 K (-40°C)	0.2K	0.7K	1.7K
Object at 293 K (20°C)	0.1K	0.4K	0.8K

Table 2: Temperature bias (K) generated by the parasite flux for Integrated flux seen by a Infratec Variocam (pW/Pixel). In red we indicate the bias larger than 5K, which would exceed the 5% error (in°C scale).

4.5. Test results

The first step in the processing was to match (space) and to synchronize (time) the measurement field with Pt100 and the corresponding thermography acquisition points (Fig.14). The temperatures are recorded by CSL acquisition system Octoplus.
The thermographic data from the Infratec VarioCam camera is processed with the IRBIS software. IRBIS records continuous thermographic pixelized images. This means 2D data sets of digital values (DV) that are becoming temperature values if one associates a camera “in-build” calibration formula.

The time sequence from IRBIS is exported in Excel format, then imported in Matlab. On the other hand, the data from the Pt100 is also exported to Excel format then re-imported in Matlab.
The Pt100 are localized with an uncertainty of 10 mm. An area of 15 by 15 pixels of about 1.4 mm width or 21 mm x 21 mm. IRBIS can compute an average value and standard deviation within that region of interest of (225 pixels).
In order to see the contribution of temporal noise, one made two types of integration.

- A sequence of 20 means and averages.
- A sequence of 20 time-averaged means and 20 time-averaged averages (time averaging in the Camera)

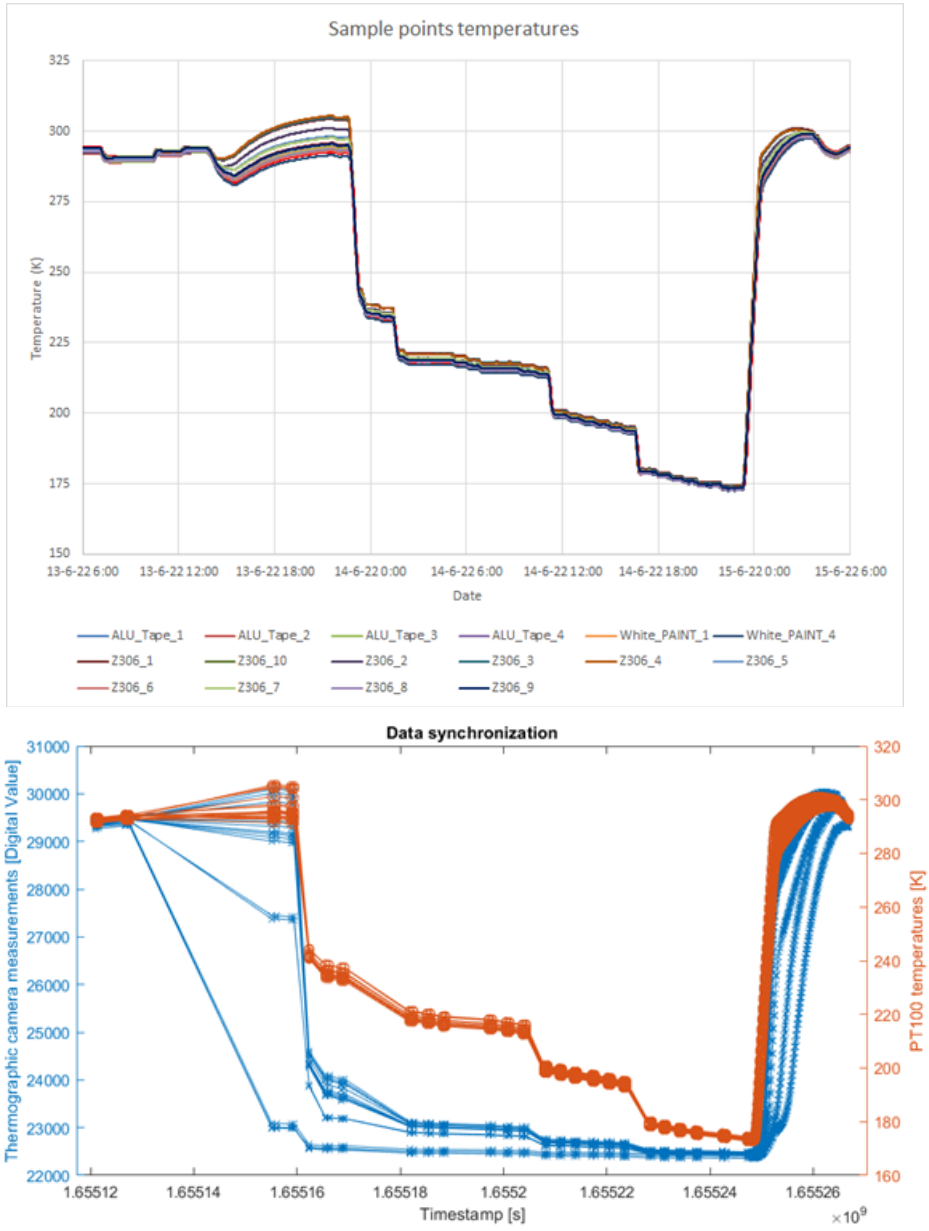

Figure 15: Synchronized plot of (above) Pt100 data on samples area and (below) corresponding data sets of the thermographic camera.

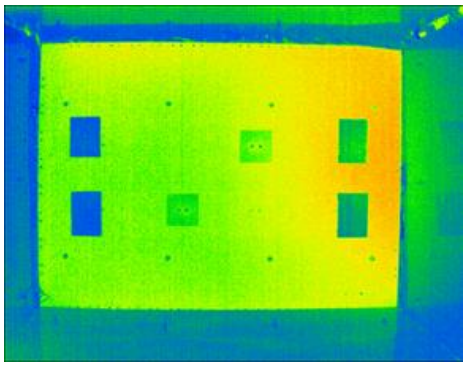

Figure 16: False color image of the set up @20°C buffer shroud 20°C.

Figure 17: False color image of the set up @20°C buffer shroud -185°C. The yellow arrow points towards regions where only self-radiation of the ballast shroud is present.

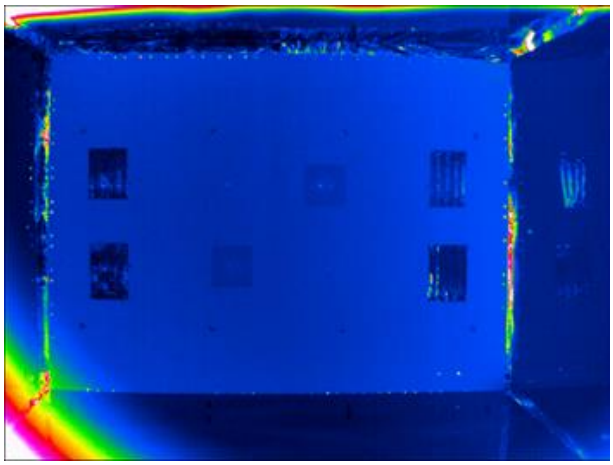

Figure 18: False color image @-100°C buffer shroud @-185°C. One notices that there is still contrasts between signal shroud and ballast shroud.

A frustration occurred when the IRBIS software (with its in build calibration) stopped providing temperatures (all temperatures blocked at -40°C). This meant that one had to record and process DV. This results in Fig.18. The processed curve shows a kink around -40°C. After discussion with JENOPTIK (manufacturer of the camera), it turned out that the provided data are proportional to radiometric flux below -40°C and are already processed above -40°C.

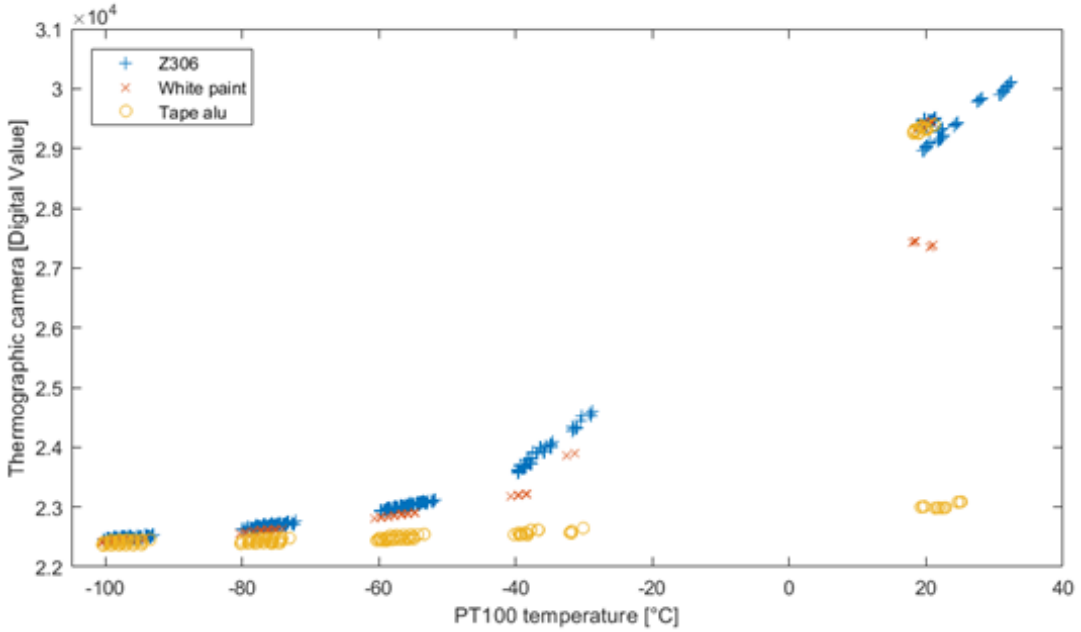

Figure 19: *Plot of the Digital Value measured by the thermographic camera as a function of the temperature of the measurement zones (Sample shroud)*

4.6. From digital values to temperature

The thermographic camera provides values, noted V, in Digital Value unit (DV) that "are said" to be proportional to the total flux, noted F, seen by each pixel of the camera. The total flux per pixel seen by the camera is the sum of multiple contribution:

$$F\_total=F\_internal+F\_W+F\_W\rho +F\_object+F\_(object\ \rho) \quad (3)$$

where:
F_internal represents the internal thermal flux coming from the camera itself, *F_W* the thermal emission of the window, *F_Wρ* the flux reflected by the ZnSe window, *F_object* the thermal emission of the sample object, and *F_(object ρ)* the flux reflected by the object. The camera is configured to perform non-uniformity correction to obtain linear response, but this operation also computes and removes the internal flux contribution. The value provided by the camera is proportional to:

$$F\_DV = F\_total-F\_internal$$

$$=F\_W+F\_W\rho+F\_object+F\_(object\ \rho) \quad (4)$$

And the camera values obtained, noted V, are given by:

$$V=G\_camera\ \ F\_DV+O\_camera \quad (5)$$

where the gain, *G_camera*, and offset, *O_camera*, are unknown. Combining Eq.4 and Eq. 5 one obtains:

$$V=E\_W+E\_W\rho+E\_object +E\_(object\ \rho)+O\_camera \quad (6)$$

Simplifying the notation by defining:

$$G\_camera\ \ F\_i=E\_i \quad (7)$$

Before the start of the test, one observed that, when all elements were at room temperature, a halo is visible on the image. This halo is produced by the internal thermal radiation of the camera reflected by the ZnSe window (Fig.13).
This contribution is taken into account in *E_Wρ* and it is split in 2 parts. One part is a uniform reflection of 21 °C, *E_(W uniform)*, the second part is the higher temperature coming from the camera, *E_(W halo):*

$$E\_W\rho=E\_(W\rho\ uniform)+E\_(W\rho\ halo)\ (x,y) \quad (8)$$

E_(Wρ uniform) is the same on every pixel of the image, but *E_(Wρ halo) (x,y)* is not.

One obtains the final equation:

$$V=E\_W+E\_(W\rho uniform)+E\_(W\rho\ halo) +E\_object+E\_(object\ \rho)+O\_camera \quad (9)$$

This halo and its non-uniformity is very difficult to simulate. One makes the hypothesis that the coldest pixel in the image (called V_{min}) of the camera is a pixel that corresponds to a thermal emission equals to the temperature of the shroud tunnel (E_(object ρ)=0). At the temperature of liquid nitrogen (~ 90 K / -185 °C) there are almost no emission in the spectral range of the detector (Fig.14). One can only identify and measure this pixel when the tunnel ballast shroud is cold.
This is a fair assumption when compared to the typical flux self-emitted by the sample objects (Tab.1). This means that one says that if a value is measured it comes from the camera halo.

$$V\_min\approx E\_W+E\_(W\rho\ uniform) +E\_(W\rho\ halo)\ (x,y)+O\_camera \quad (10)$$

This value, does not estimate correctly *E_(Wρ halo) (x,y)* because it only take the contribution in a single pixel. For estimating, *E_(Wρ halo) (x,y)*, the acquisitions where all elements were at room temperature is considered, and the difference on every measurement zones is computed. One defines a list a values difference, noted ⟦ΔV⟧_i where i= 1,2,3… Then one obtains:

$$V\approx\langle V\_min\ \rangle+⟦\Delta V⟧\_i+E\_object+E\_(object\ \rho) \quad (11)$$

where $\langle V\_min\ \rangle$ is the value of V_min averaged on all acquisitions with cold buffer shrouds. It is worth noting that ⟦ΔV⟧_i is different for every measurement zone (area of interest). One defines $V\_offset\ (x,y)=\langle V\_min\ \rangle+\Delta V(x,y)$ to simplify the equation:

$$V\approx V\_offset\ (x,y)+E\_object+E\_(object\ \rho) \quad (12)$$

E_(object ρ), (for high emissivity objects one makes probably flux errors of< 1% , but 10% for reflective objects), thus the equation becomes:

$$E\_object\approx V-\langle V\_min\ \rangle-⟦\Delta V⟧\_i \quad (13)$$

If one reverts the simplification from Eq.5:

$$⟦G\_DV\ F⟧\_object\approx V-\langle V\_min\ \rangle-⟦\Delta V⟧\_i \quad (14)$$

Defining BB(T) as the flux of thermal radiation of a black body at temperature T, one has:

$$F\_object=\varepsilon\ BB(T) \quad (15)$$

where ε is the emissivity of the object.

Combining Eq.13 and Eq.14, one defines:

$$⟦BB⟧\_DV\ (T)=G\_DV\ \ BB(T) \approx 1/\varepsilon\ [V-\langle V\_min\ \rangle-⟦\Delta V⟧\_i\ ] \quad (16)$$

This equation allows to obtain an estimation of the

black body radiation corresponding to Digital Value **when the emissivity is known**.
For every measurement zone, T is known and value of ⟦BB⟧_DVcan be computed. The emissivity values are:

- Z306 ε = 88 %
- White paint ε = 80 %
- Aluminum tape ε = 20 %

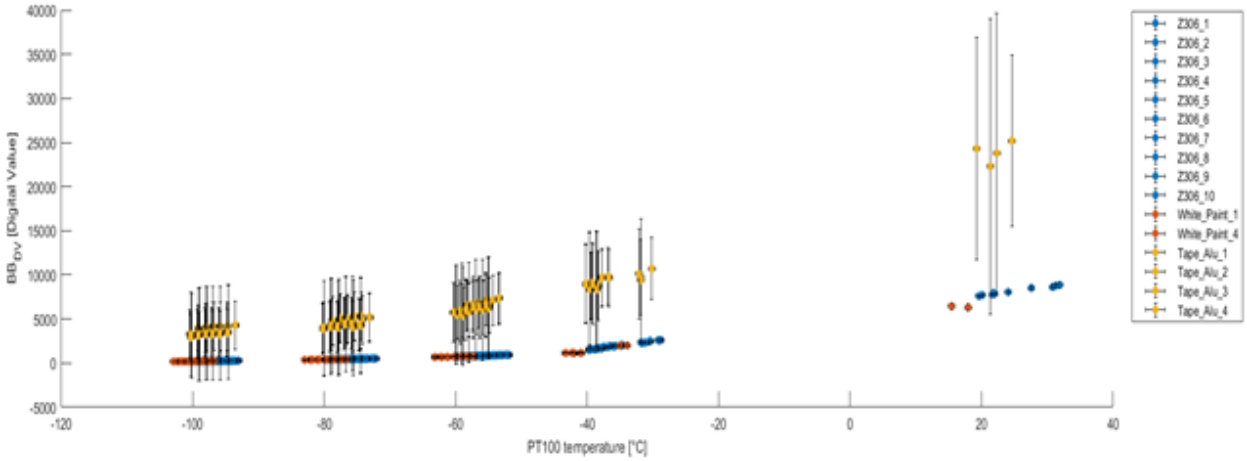

Figure 20: Black body value in Digital Value as a function of temperature

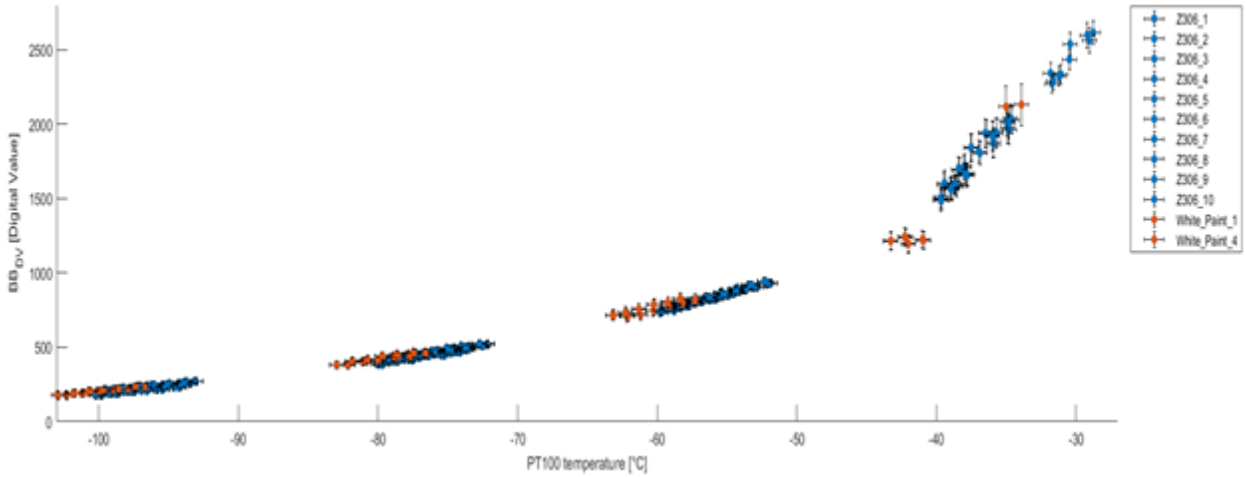

Figure 21: Black body value in Digital Value as a function of temperature, for the 4 cold plateaus, of the Chemglaze and White paint objects

For the error bars, we use the StDv provided by IRBIS for the different measurement zones at different temperatures, noted σ_i (T):

$$⟦error(T)⟧_i=(2\ \sigma_i\ (T))/\varepsilon \quad (17)$$

The relationship between temperature and digital value seems to be proportional only in the calibration range -40°C to +120 °C. Below -40 °C, there is a clear limit of the linear behaviour, and the relationship is no longer linear.
One fitted the calibrated part (-40 to 120 °C) with the linear fit:

$$⟦BB⟧_DV\ (T)=a.(T+273.15)+b \quad (18)$$

Only Z306 and white paint have been used for the fit, because Aluminium tape error bars are too large.
Computed fit parameters are:

$$a=102.7,\ b=-22462 \quad (19)$$

with R-squared=0.9994 and a RMS error of 60.8.

Below -40 °C, one used an exponential fit:

$$⟦BB⟧_DV\ (T)=a.exp(b.(T+273.15))+c \quad (20)$$

Computed fit parameters are:

$$a=2.90,\ b=0.0265,\ c=-74.5 \quad (21)$$

with R-squared=0.9947 and a RMS error of 18.6.
The intersection of both fit happens approximatively at T = - 42 °C and BBDV = 1210 DV.

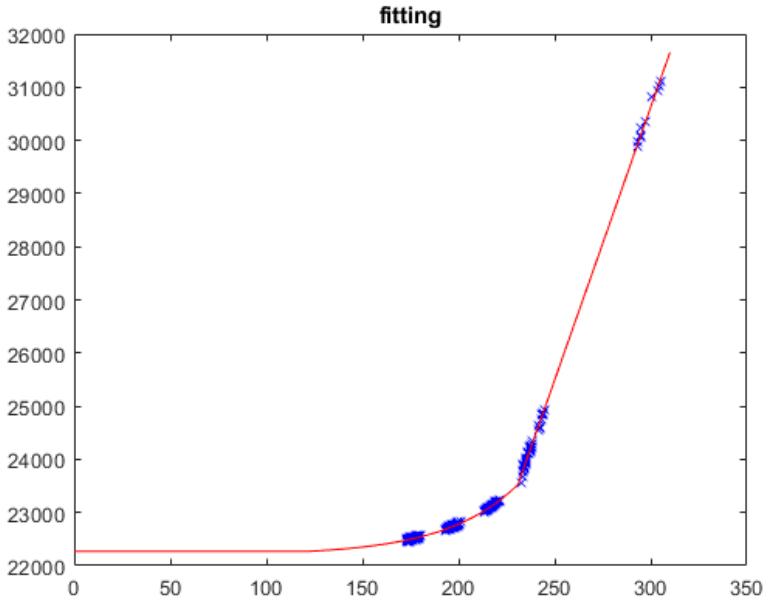

Figure 22: Fitting of the temperature as a function of digital value

One can now use $[BB]\_DV\ (T)$ to convert DV measurement from the camera to temperature estimation.
For this, one uses the measurements of the shroud temperature in the vacuum facility (T_shrouds+273.15) and the object emissivity (ε):

$$T_{object} = BB_{DV}^{-1}\left[\frac{DV-(1-\varepsilon)BB_{DV}(T_{shrouds}+273.15)}{\varepsilon}\right] \quad (22)$$

Where $BB_{DV}^{-1}(v)$ is the inverse function of $BB_{DV}(T_{object})$:

$$BB_{DV}^{-1}[BB_{DV}(T)] = T \quad (23)$$

At low temperatures (i.e. below -40 °C), $BB_{DV}(T)$ is given by equation (18). To estimate temperature precision, we take the derivative:

$$\frac{dBB_{DV}(T)}{dT} = ab\ e^{b\ (T+273.15)} \quad (24)$$

The temperature precision estimation based on the variation of $BB_{DV}(T)$:

$$dT = \frac{dBB_{DV}(T)}{b[\boldsymbol{BB}_{DV}(T)-c]} \quad (15)$$

Fig.22 shows the value of $dBB_{DV}(T)$ is based on the StDv values provided by the IRBIS software. The mean value of all StDv is 9.93 DV. That represents 64 % of the measurement points. For 95 % of measurements, one has to take double StDv. One obtains temperature measurement precision estimation in Fig.23.

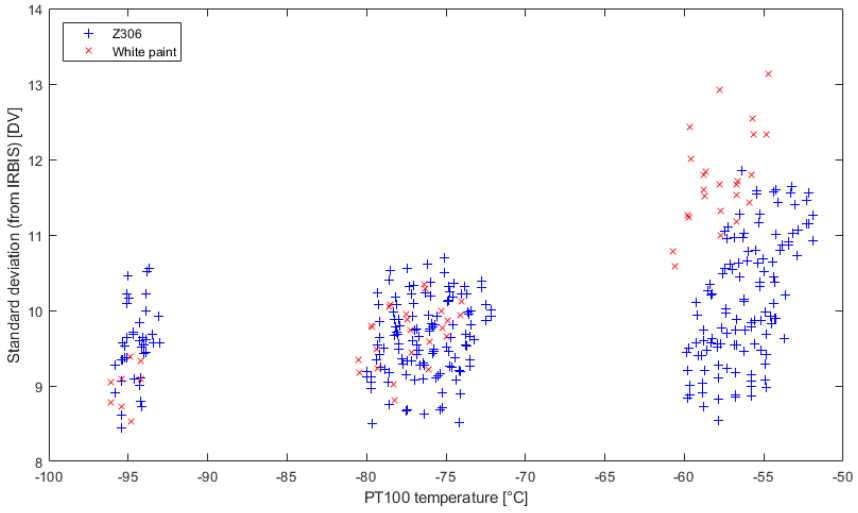

Figure 23: Standard deviation of Digital Value measured for Z306 (blue) areas and white paint (red) areas

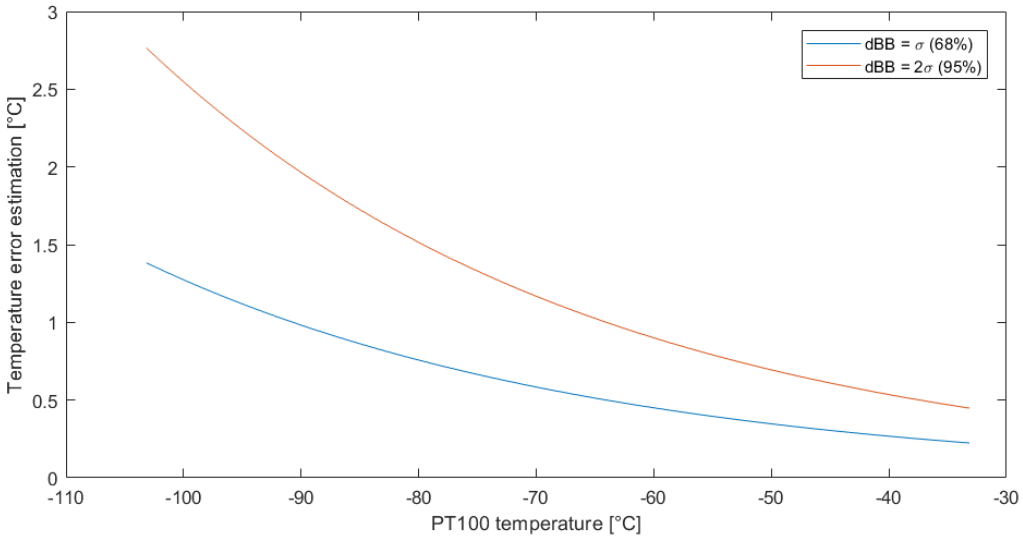

Figure 24: Estimation of temperature measurement resolution achievable by the Infratec VarioCAM HD camera

This data can be used to make an absolute temperature measurement model.

$$\Delta T = RSS(A,B,C)$$

- A: error on the traceable part of the treaceable part of the measurement: the Pt100 uncertainty is 0.5°C
- B: camera noise part $\Delta(\Delta t, T_{detector})$ => this the prediction of Eq.22 , consider a constant dBB(T)=2*20
- C: 0.5% T_{object} => Is the model uncertainty due to emissivity $\Delta T \div T.\Delta\varepsilon/(4.\varepsilon)$

-
- Below -40°C

$$\Delta T = \sqrt{(0.5°C)^2 + (20/(0.0785.e^{0.0265.(T+273.15)}))^2 + (0.005(T+273.5))^2}$$

Above -40°C

$$\Delta T = \sqrt{(0.5°C)^2 + (20/(102.7))^2 + (0.005(T+273.5)))^2}$$

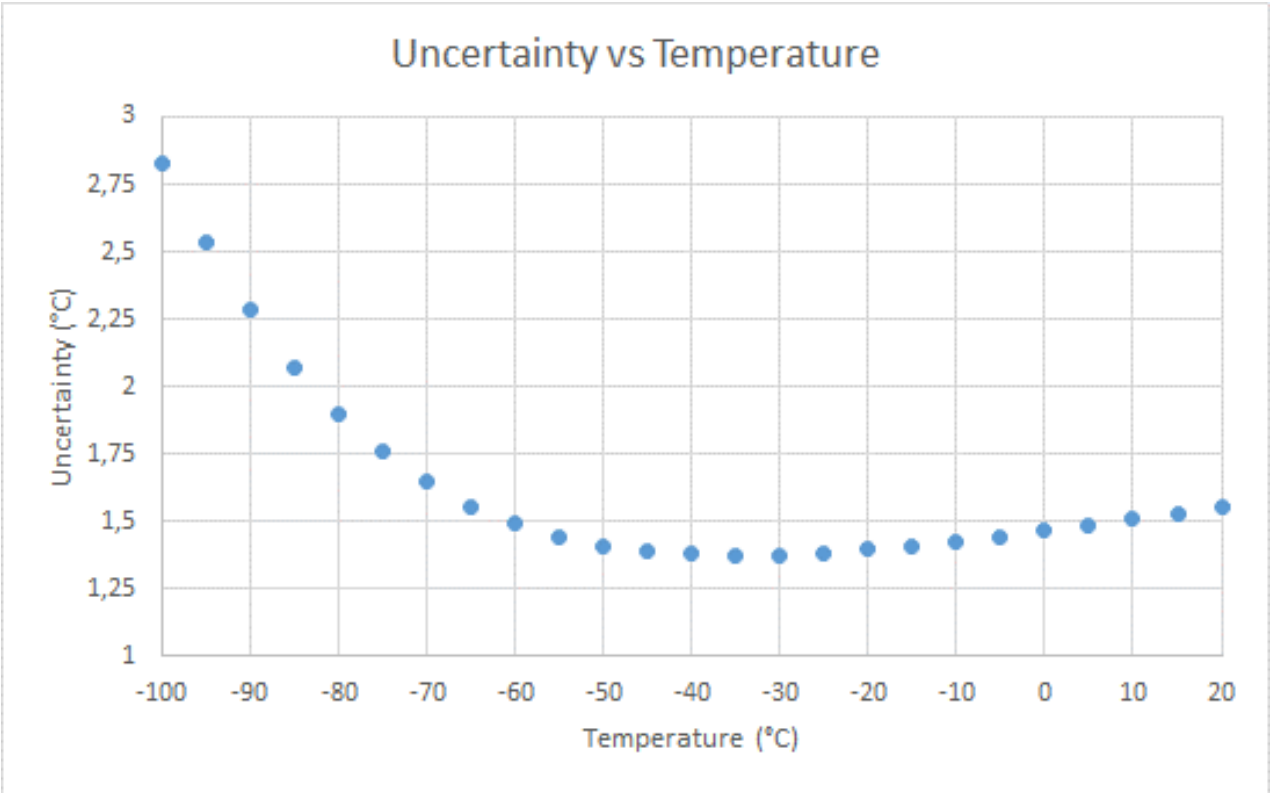

Figure 25: Estimation of temperature uncertainty based on the 'estimation' model and high emissivity object, measured with Infratec Variocam camera.

5. CONCLUSIONS

The present activity has assessed the feasibility to measure, using a thermographic camera, object temperatures in thermal vacuum conditions and cooled down to -100°C.
The demonstration has shown that this is possible using commercial uncooled microbolometer thermal imagers, because of their large spectral sensitivity towards large wavelengths.

The test geometry and test configuration require some precautions, which is to control – eventually eliminate – parasite heat fluxes reflected by the object under test. These parasite fluxes can clearly be a showstopper for the temperature measurement of low emissivity objects. Note that one detected very low fluxes on low emissivity objects. However, the uncertainty (error bar is large).

Thermal flux differences were measured, and they were significant to resolve temperature difference of 2K@ 100°C for high emissivity objects.
The exercise eventually turned into the construction of a temperature estimation model and assessment of measurement uncertainty, traced with respect to temperature measured on the object under test.

This is mainly due that infrared thermal imagers aim applications with temperature range higher than -40°C and some practical issues were encountered:

- There are no calibration facilities to calibrate the camera flux for temperatures lower than -40°C.
- Software limits the measured flux, considered as non-significant.

One recommends that the calibration software (flux to temperature conversion) shall be made available by camera manufacturers, or at least that calibration routines can interact with the camera.
Indeed, this has currently prevented to provide a direct temperature value in this activity. The camera was not calibrated lower than -40°C, and the calibration curve could not be extrapolated towards lower temperature [7].

A proper temperature measurement system down to -100°C can only be reliable if:

- The camera is characterized and optimized (choice op systems sensitivity) for temperature lower than -40°C.
- The camera is calibrated for temperature from 80°C to -100°C. This includes camera, with correct lens, integration time, F/# number, without or without viewport (ZnSe window) and operating at the representative environmental temperature (canister).
- The parasite fluxes (flux offset) are measured in the test environment and subtracted from the raw data.
- Averaging routines and statistics are implemented to assess the data quality of thermographic imagers.
- A presence of some physical sensors (Thermocouples or thermistances) and in situ re-calibration are assets.

6. ACKNOWLEDGEMENT

This work was performed under ESA contract 4000136454/21/NL/MG/zk

7. REFERENCES

[1] Gianluca Casarosa, Matteo Appoloni, INFRARED Emissivity Test Bench, 27th Aerospace Testing Seminar, October 2012.
[2] Attila Jasko, New Generation IR cam for TVAC - Operational Instructions, ESA-TEC-MXE-THER-INST-00203 (2021)
[3] Attila Jasko, Gianluca Casarosa, Matteo Appolloni, Retrofitting of a COTS IR Camera for Thermal-Vacuum Testing 32nd Aerospace Testing Seminar, (2021)
[4] Anis Redjimi et al., Noise Equivalent Temperature Difference Model for Thermal Imagers, Calculation and Analysis, Scientific Technical Review, 2014,Vol.64,No.2,pp.42-49.
[5] D.i Todaka, Development status of thermal-vacuum test-applicable IR camera, 64th AIAA_presentation.
[6] NASA/TP-2005-212792, Spacecraft Thermal Control Coatings References, Lonny Kauder
[7] Infratec Variocam calibrartion certificate3372/2022